PHYSICAL SCIENCES

Liquid film–induced critical heat flux enhancement on structured surfaces

Jiaqi Li[1], Daniel Kang[1], Kazi Fazle Rabbi[1], Wuchen Fu[1], Xiao Yan[1], Xiaolong Fang[1], Liwu Fan[2], Nenad Miljkovic[1,3,4,5]*

Enhancing critical heat flux (CHF) during boiling with structured surfaces has received much attention because of its important implications for two-phase flow. The role of surface structures on bubble evolution and CHF enhancement remains unclear because of the lack of direct visualization of the liquid- and solid-vapor interfaces. Here, we use high-magnification in-liquid endoscopy to directly probe bubble behavior during boiling. We report the previously unidentified coexistence of two distinct three-phase contact lines underneath growing bubbles on structured surfaces, resulting in retention of a thin liquid film within the structures between the two contact lines due to their disparate advancing velocities. This finding sheds light on a previously unidentified mechanism governing bubble evolution on structured surfaces, which has notable implications for a variety of real systems using bubble formation, such as thermal management, microfluidics, and electrochemical reactors.

INTRODUCTION

The boiling process is of vital importance to the success of many processes due to the utilization of the latent heat to achieve extremely efficient thermal transport and continual fluid agitation stemming from bubble formation and departure, which enhances mass transfer (*1*). Bubble formation is critical to boiling heat and mass transfer. During nucleate pool boiling, a bubble generates on an activated nucleation site and proceeds to expand rapidly, leaving a dry spot underneath the bubble surrounded by the three-phase contact line and liquid microlayer. During the bubble ebullition cycle, the surrounding liquid rewets the dry spot to compensate for the evaporated liquid, thereby maintaining a delicate balance between evaporation and replenishment. Once this balance is disturbed, the surrounding liquid is prevented from rewetting dry areas, resulting in a drastic decrease in heat transfer efficiency. This critical value, termed the critical heat flux (CHF), governs the maximum heat transfer capacity possible from the surface to the liquid. Therefore, the fundamental and complete understanding of bubble dynamics during boiling has been central to the design and operational safety of many processes (*2*).

In the past century, surface properties, such as roughness, porosity, wettability, and wickability, have all proven effective at regulating replenishment of liquid during the ebullition cycle, thereby altering CHF (*3*–*8*). To date, various structured surfaces with microstructures (*9*–*11*), nanostructures (*12*–*15*), and hierarchical micro/nanostructures (*16*–*22*) have been adopted to regulate bubble behavior. Numerous mechanisms have been proposed to illustrate liquid replenishment enhancement during ebullition (*2*), mainly focusing on the augmentation of the liquid-solid contact area (*10*), liquid retention (*23*, *24*), and capillary wicking (*25*–*27*). To obtain a better understanding of the role of bubble dynamics on CHF enhancement, various techniques, such as laser interferometry (*11*, *28*, *29*), infrared thermography (*18*, *30*–*33*), and x-ray imaging (*27*), have been used to probe the dry area beneath growing and departing bubbles. Although understanding of the role of surface structures on bubble dynamics has progressed, the mechanistic understanding of liquid replenishment during bubble evolution remains poorly understood because of difficulty in observing the liquid-vapor interface.

Using high-magnification in-liquid endoscopy, we directly observe that structures on the surface retain liquid during bubble expansion, forming a thin liquid film underneath the bubble. The previously unobserved retained liquid film is formed during the initial stage of bubble growth and is not present on smooth surfaces. As the bubble continues to grow because of the evaporation, the retained liquid film dries out, forming a second three-phase contact line that gradually spreads outward until the entire film disappears. We show that the first-tier three-phase contact line forms on the structures and is caused by bubble expansion, while the second-tier three-phase contact line forms within the structures and is governed by advancing liquid film dynamics. We study this interesting contact line phenomenon by experimentally probing bubble dynamics on various structured surfaces to elucidate its role on CHF via a modified hydrodynamic instability model.

RESULTS

To investigate bubble dynamics on structured surfaces, single-tier and hierarchical micro/nanostructures with various characteristic length scales and thicknesses were prepared. Structures with nanoposts or pores have the capacity to sustain thin liquid films through capillarity (*34*). Therefore, we designed and prepared structures on copper (Cu) substrates using chemical etching, forming nanograss, nanobuds, nanoflowers, and nanopetals, as shown in Fig. 1 (A to H) (see Materials and Methods and section S1). The fabricated structures were rationally chosen due to their differing characteristic length scales and heights (thickness), resulting in distinguishable capabilities for liquid retention. Each layer thickness was estimated using focused ion beam (FIB) sectioning and is shown in Fig. 1I, demonstrating variation from 2 to 12 μm. Surface chemistry analysis of both unmodified and modified surfaces was conducted using

[1]Department of Mechanical Science and Engineering, University of Illinois at Urbana-Champaign, Urbana, IL 61801, USA. [2]Institute of Thermal Science and Power Systems, School of Energy Engineering, Zhejiang University, Hangzhou 310027, China. [3]Department of Electrical and Computer Engineering, University of Illinois at Urbana-Champaign, Urbana, IL 61801, USA. [4]Materials Research Laboratory, University of Illinois at Urbana-Champaign, Urbana, IL 61801, USA. [5]International Institute for Carbon Neutral Energy Research (WPI-I2CNER), Kyushu University, 744 Moto-oka, Nishi-ku, Fukuoka 819-0395, Japan.
*Corresponding author. Email: nmiljkov@illinois.edu

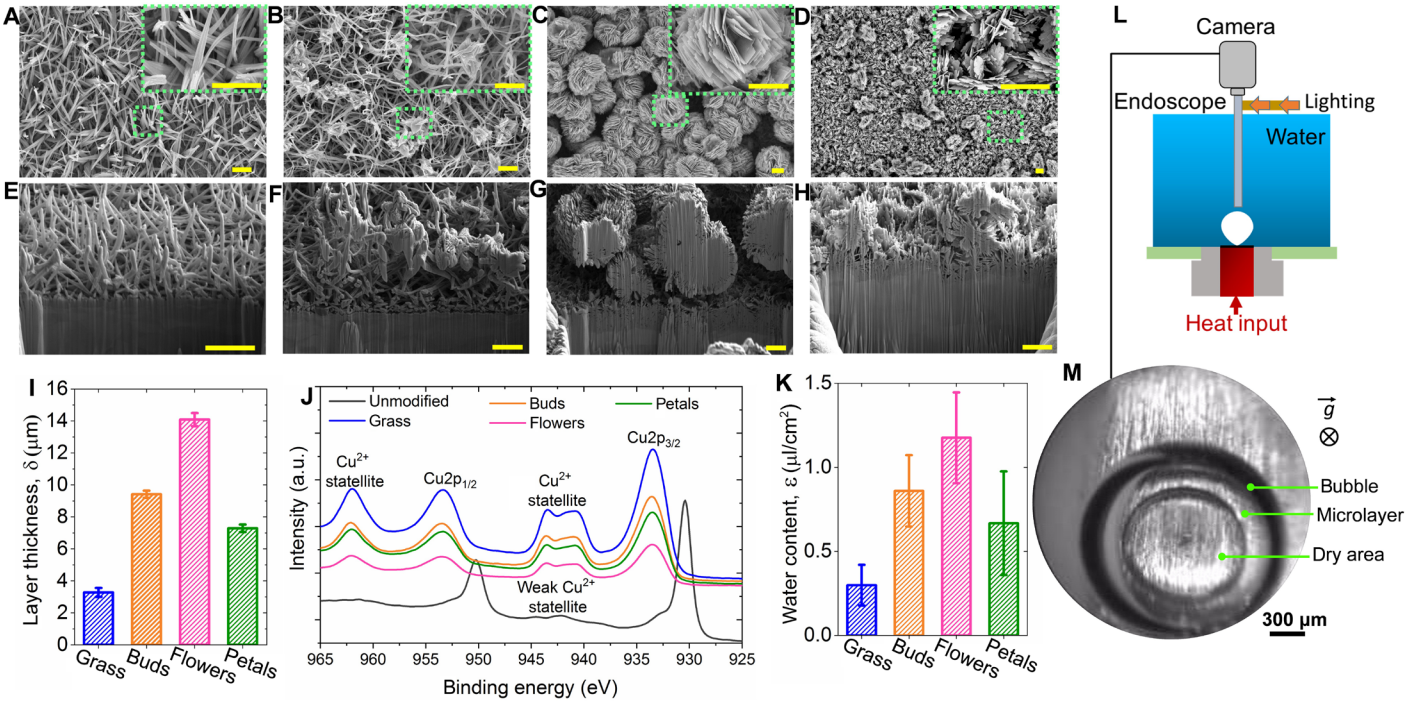

Fig. 1. Experimental pool boiling methodology. Scanning electron microscopy (SEM) images of Cu-structured surfaces having CuO structures with (**A**) nanograss, (**B**) nanobud, (**C**) nanoflower, and (**D**) nanopetal morphologies. The dotted green regions in (A) to (D) represent the length scale observed in their upper right corner insets. Focused ion beam (FIB) cross-sectional images of the CuO structures with (**E**) nanograss, (**F**) nanobud, (**G**) nanoflower, and (**H**) nanopetal morphologies. (**I**) Structure layer thickness, (**J**) high-resolution x-ray photoelectron spectroscopy (XPS) spectra of Cu 2p, and (**K**) water content (ε) for the different structured surfaces. Details of the surface fabrication can be found in Materials and Methods. (**L**) Schematic diagram of the pool boiling experimental setup. A high-magnification endoscope with a high-speed camera was used to observe in situ and in-liquid bubble dynamics from the top. (**M**) Exemplary endoscopic snapshot of a single bubble on an unmodified Cu surface at a heat flux of 17.7 W/cm^2. Scale bars of (A) to (H), including insets, represent 2 μm. a.u., arbitrary units.

x-ray photoelectron spectroscopy (XPS) (see Materials and Methods). The presence of the Cu (II) oxidation state is visible from Fig. 1J. The high-resolution XPS spectra of Cu 2p, consisting of strong Cu^{2+} satellite features as well as broader Cu $2p_{1/2}$ and Cu $2p_{3/2}$ peaks compared to the regular Cu surface, illustrate the presence of CuO on the surface.

Water content, quantified as the volume of retained water in the structure per unit normalized face area, varies with structure thickness and characteristic length. To quantify water content, we adopted the preparation method of lubricant-infused surfaces (*35*) in which a low-surface energy nonreacting liquid lubricant is injected and stabilized in the structures by capillarity. The pores of the structures were filled with a lubricant, enabling the characterization of the volume of the lubricant per unit area. Vacuum-grade Krytox lubricant (Krytox VPF 1525) having a high density and dynamic viscosity with low vapor pressure was chosen (see Materials and Methods) to increase signal-to-noise ratio in the mass measurement, limit mass loss due to evaporation, and ensure complete filling of pores with limited gravitational drainage after removal of excess lubricant. As illustrated in Fig. 1K, the water content (ε) variation of the fabricated structures showed a clear trend, which demonstrated that thicker structures have enhanced capacity for liquid retention.

Having characterized the surface structure morphology and water content, we used a customized high-magnification endoscopic system to visualize in situ and in-liquid three-phase interface behavior during pool boiling of water. A schematic of the experimental rig with an exemplary image of a single bubble captured by endoscopy is shown in Fig. 1 (L and M). Distilled water [Chemical Abstracts Service (CAS) no. 7732-18-5, Aqua Solutions] was used as the working fluid, and all experiments were carried out at saturation conditions at atmospheric pressure ($T_{sat} \approx 100$°C, Urbana, IL). A detailed description of the experimental setup with a full uncertainty analysis can be found in Materials and Methods and section S1.

Pool boiling performance was characterized by measuring the boiling curve, defined as the surface heat flux (q'') as a function of the wall superheat (ΔT_{sat}), and the heat transfer coefficient (HTC) curve, defined as the heat transfer coefficient (h) as a function of surface heat flux (q''). Pool boiling experiments on both unmodified and structured surfaces were conducted, with boiling and HTC curves shown in Fig. 2 (A and B). The CHF on the unmodified Cu surface was 116 ± 4 W/cm^2, consistent with past experiments and the predicted value on an infinite flat surface based on hydrodynamic instability (≈110 W/cm^2) (*36*). Regardless of the structure morphology, the existence of structures notably improved the CHF and HTC compared with the unmodified surface. The nanoflower structures showed the highest CHF, $q'' \approx 300 \pm 6.8$ W/cm^2 at $\Delta T_{sat} \approx 27.7 \pm 2.4$°C, resulting in $h \approx 108 \pm 11$ kW/(m^2·K). The CHF enhancement varied with the structure morphology. As the nanograss life cycle evolved from grass to petals, the CHF enhancement first gradually increased to a maximum and then decreased (Fig. 2C). Considering the variation of water content for each structure (Fig. 1K), we observe that CHF enhancement is proportional to water content. As illustrated in Fig. 2D, the CHF shows a linear monotonic increase with increasing water content (ε) for the structures considered here.

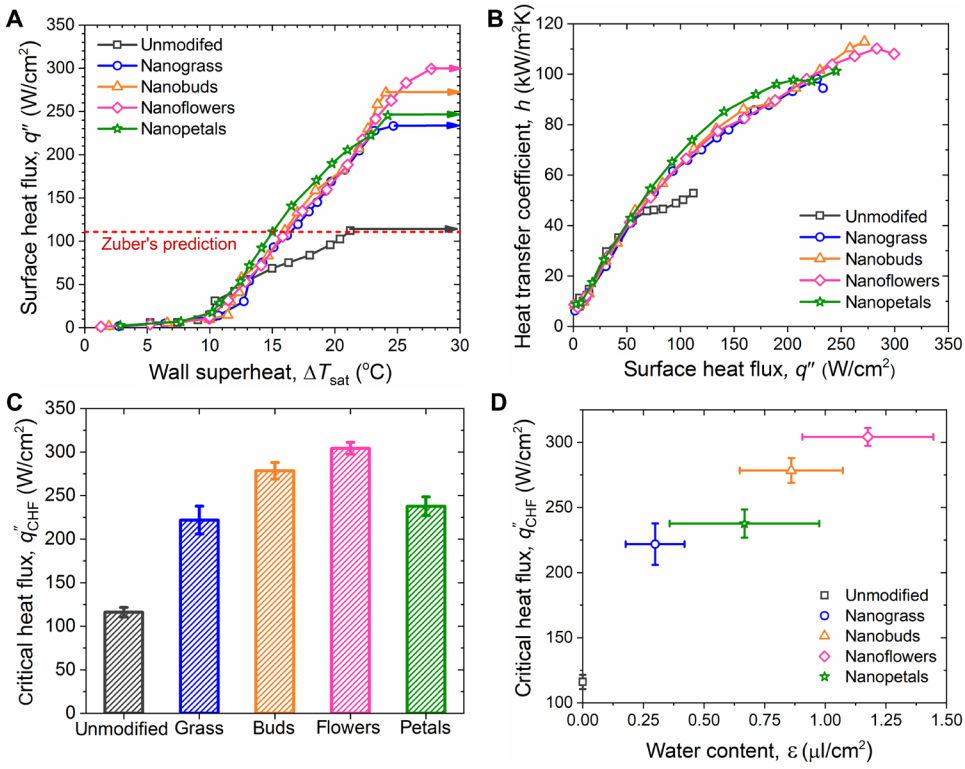

Fig. 2. Boiling heat transfer characterization. Experimentally measured (**A**) boiling surface heat flux (q'') as a function of wall superheat ($\Delta T_{sat} = T_{wall} - T_{sat}$) and (**B**) boiling heat transfer coefficient (h) as a function of q'' for the structured surfaces (Fig. 1). Arrows pointing to the right in (A) represent CHF. Experimentally measured (**C**) CHF on the different structured surfaces (Fig. 1) and (**D**) CHF as a function of water content (ε, Fig. 1K). Error bars in all plots represent propagated uncertainty of the measurements (section S1).

To understand the mechanisms regulating pool boiling performance and to clarify the relationship between the bubble dynamics and CHF, a variable magnification endoscope was used to observe bubble behavior in situ during pool boiling. To enable high-magnification imaging of single bubble growth, the surface heat flux during observation was restricted to $q'' \approx 20 \pm 4$ W/cm^2, where nucleate boiling is in the isolated bubble regime, and bubbles grew individually and rarely coalesced with the surrounding bubbles. Furthermore, the surface heat flux during observation was higher than the heat flux at the onset of nucleate boiling for both unmodified and modified structured surfaces, which increased the number of activated nucleation sites. To avoid the influence of potential outliers stemming from low data population, bubbles generated at different spatial locations were selected for statistical analysis. All values related to bubble growth, such as evaporation time of the liquid film and area of dry spot underneath the bubble, are statistical averages of 10 bubbles on at least five different spatially varying nucleation sites. At higher heat fluxes, the density of nucleation sites increased, raising the possibility of bubble coalescence during growth and additional complexity for interface analysis. Given that the main contributor to increased heat flux during pool boiling is the activation of nucleation sites and that the average bubble departure diameter and frequency for a particular surface structure have a relatively weak sensitivity to surface heat flux, analysis of bubble dynamics at reduced heat fluxes reflects the heat transfer mechanisms occurring at higher heat fluxes (*17*, *23*, *37*).

A schematic diagram with top-view optical images of bubble dynamics on an unmodified and a structured nanograss surface is shown in Fig. 3 (A to D) (movies S1 and S2). On the unmodified surface, a bubble first generated in a cavity, which was activated as a nucleation site at τ = 0 ms (Fig. 3, A and B, i). The bubble subsequently expanded rapidly by evaporation of the surrounding superheated liquid. Because of vigorous evaporation, dry-out occurred near the defect, creating a dry spot in the center of the bubble base (Fig. 3, A and B, ii). With continued bubble growth, the surrounding liquid was pushed away, leaving a small amount of liquid surrounding the dry spot beneath the bubble, termed the microlayer (Fig. 3, A and B, iii). The interface along the dry spot at the vapor bubble/microlayer region is known as the three-phase contact line. Because of the low resistance to heat conduction through the microlayer in the out-of-plane thickness direction, evaporation in this region is rapid, providing most of the energy required for bubble growth. During the bubble growth process from τ = 0 ms (Fig. 3, A and B, i) to τ = 3.0 ms (Fig. 3, A and B, iii), the three-phase contact line advanced via the complete evaporation of the microlayer, leading to the outward propagation of the dry spot. At τ = 3.0 ms (Fig. 3, A and B, iii), the dry spot area reached its maximum extent. As the bubble continued to grow (τ > 3.0 ms), it moved upward (out of the page) due to buoyancy, while the three-phase contact line receded toward the center of the bubble base, resulting in shrinkage of the dry spot (Fig. 3, A and B, iv). During this process, liquid returned to rewet the superheated dry spot, initiating quenching. At τ = 12.1 ms, the

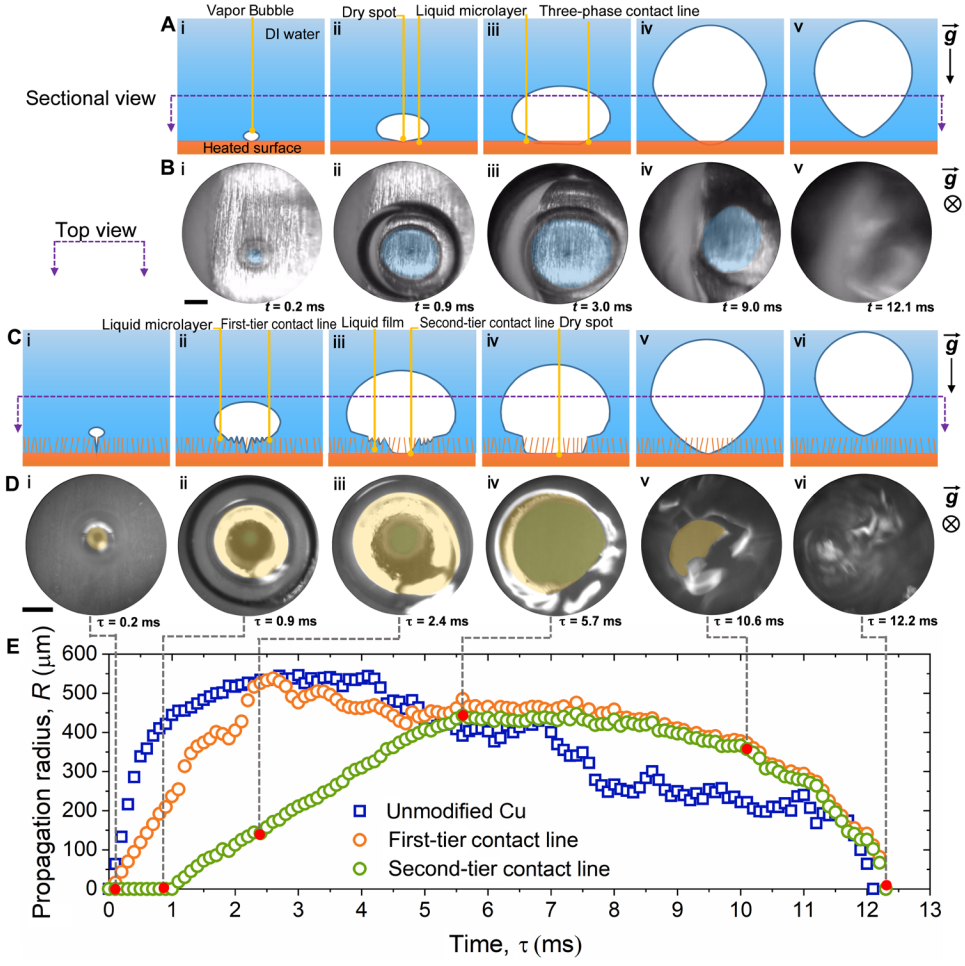

Fig. 3. In situ endoscopy of bubble and contact line dynamics. (**A**) Sectional-view schematic with (**B**) top-view endoscopy photographs of bubble evolution on an unmodified Cu surface. (**C**) Sectional-view schematic and (**D**) top-view endoscopic photographs of bubble evolution on the structured nanograss surface. Scale bars in (B) and (D) represent 300 μm. (**E**) Transient advancing contact line propagation radius (*R*) on the unmodified surface and the first-tier and second-tier contact line radii on a nanograss surface. Time zero (τ = 0) represents when the bubble was generated. The surface heat fluxes for the two corresponding images in (B) and (D) are ≈17.7 ± 3.5 W/cm^2 and ≈20.3 ± 1.8 W/cm^2, respectively. Error bars in (E) are smaller than the data symbols and are not shown for clarity. Top-view high-speed videos of bubble and contact line dynamics on both unmodified (movie S1) and structured surfaces with nanograss (movie S2), nanobud (movie S3), nanoflower (movie S4), and nanopetal (movie S5) morphologies can be found in the Supplementary Materials.

bubble departed from the surface and the dry spot was completely rewet by the surrounding liquid. The cavity was filled with liquid from the periphery and served as a renucleation site (Fig. 3, A and B, v).

The bubble growth and departure on the structured CuO surfaces differ from the unmodified Cu surface. As shown in Fig. 3 (C and D) (movie S2), the bubble nucleates in a microscale defect of the structures at τ = 0 ms (Fig. 3, C and D, i), subsequently expanding with the same radial velocity as observed on the unmodified Cu surface. However, due to the high liquid absorption capability and large Laplace pressure barrier (capillary wicking) created by the structures, propagation of the three-phase contact line within structures is hindered. Instead, the contact line advances outward rapidly on top of the structures, leaving behind a thin liquid film inside the three-phase contact line where the dry spot on the unmodified Cu smooth surface existed (Fig. 3, C and D, ii). Here, we define the three-phase contact line as the intersection between the vapor, bulk liquid, and top of the filled structures and, henceforth, refer to it as the first-tier contact line. As the bubble continues to grow, the thickness of the liquid film near the nucleation site thins because of evaporation until a dry spot appears on the substrate. Subsequently, a second-tier three-phase contact line within the bubble base, defined by the intersection of the dry structured surface, liquid-filled pores, and vapor, appears (Fig. 3, C and D, iii). The average propagation radii (*R*) of the contact line on the unmodified Cu surface and the first-tier and second-tier contact lines on the nanograss CuO surface are shown in Fig. 3E. Both the contact line of the unmodified Cu surface and the first-tier contact line of the nanograss surface propagate rapidly outward at the initial stages of bubble growth from τ = 0 ms to τ = 2.6 ms. The bubbles expand upward, and the contact lines gradually shrink until they disappear. However, for the second-tier contact line on the nanograss surface during initial stages from τ = 0 ms to τ = 1 ms, no dry spot under the bubble base was observed. After the second-tier contact line appeared at τ = 1 ms, the dry spot gradually increased in size with continuous evaporation of the liquid film from the structure pores, leading to the linear increase of average propagation radius of the second-tier

contact line (Fig. 3, C and D). At τ = 5.7 ms, the second-tier contact line advanced outward to almost reach the first-tier contact line, with the liquid film layer in the structures completely disappearing due to evaporation (Fig. 3, C and D, iv). Because of capillary wicking from the bulk liquid to the dry area within the structures, the second-tier contact line contracts slightly relative to the first-tier contact line, leaving a stable capillary-induced liquid film ring between the two three-phase contact interfaces as observed from top-view endoscopy (Fig. 3, C and D, iv). This observation is consistent with previous studies using optical (*37*) and x-ray imaging (*27*). After τ = 5.7 ms, the bubble continues to grow, while the dry spot size and average propagation radius of the two contact lines remain approximately equivalent. At τ > 10 ms (Fig. 3, C and D, v), the bubble moves upward and departs from the surface. The three-phase contact line recedes toward the center of the bubble base, resulting in rapid shrinkage of the dry spot and the propagation radius of the contact line. Top-view high-speed videos of bubble and contact line dynamics on both unmodified (movie S1) and structured surfaces with nanograss (movie S2), nanobud (movie S3), nanoflower (movie S4), and nanopetal (movie S5) morphologies can be found in the Supplementary Materials.

The evaporation-mediated reduction of the dry spot area during bubble growth contributes to CHF enhancement. The transient dry spot propagation area (A_d) from initiation to maxima for all structured surfaces is shown in Fig. 4A. As the second-tier three-phase contact line advances in the early stage of bubble growth, the transient dry areas for all structured surfaces increase linearly with time, indicating that the propagation velocity for each surface is similar. When the thin liquid film completely evaporates, the dry spot propagation area reaches its maxima (A_{dm}). The evaporation time of the liquid film (τ_0) for different structures, defined as the time taken from the beginning of propagation to reach the maximum propagation area, varied from 4.7 to 6.1 ms. Snapshots at maximum propagation radii for the different structures are shown in Fig. 4 (D to G). The difference in liquid capacity of the structures governs their resistance to dry spot propagation. The experimental data show that the maximum dry area for the nanograss with the lowest CHF (Fig. 2C) is the largest among all of the studied structured surfaces. The nanoflower case showed the smallest dry area. To demonstrate the relationship between maximum dry area and CHF, statistical tendency analysis of CHF as a function of maximum dry spot propagation area was conducted via analysis of 100 individual bubbles for each surface, with the results shown in Fig. 4B. The CHFs obtained on both unmodified and structured surfaces have a clear inverse correlation with the maximum dry spot propagation area during bubble growth, which is caused by the variations of bubble departure diameter on the different structured surfaces. During nucleate pool boiling, the bubble departure diameter is determined by the equilibrium between buoyancy and surface tension forces, which are both functions of contact angle and dry area (*38*, *39*). Here, all of the structured surfaces are superhydrophilic, having apparent receding contact angles approaching zero. Therefore, bubbles formed

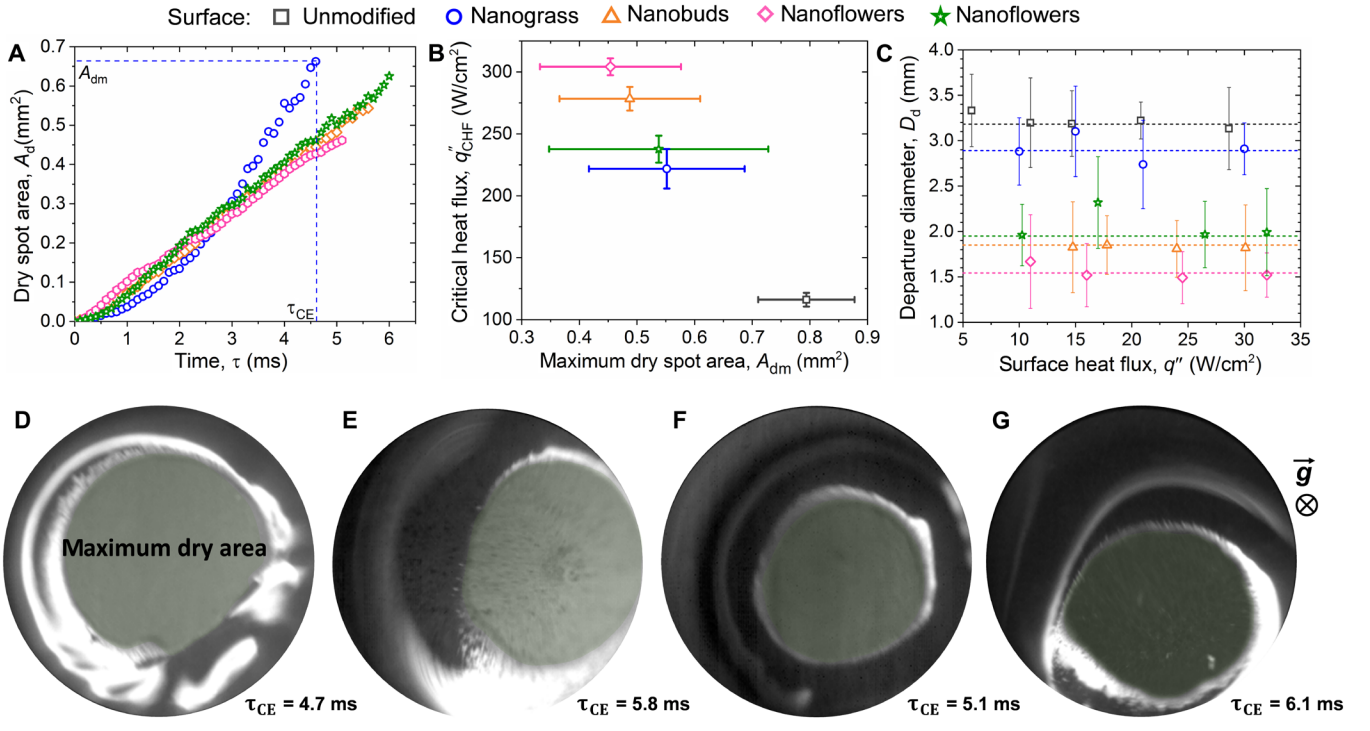

Fig. 4. Characteristics of liquid film evaporation beneath individual bubbles. (**A**) Transient dry spot propagation area (A_d) for all structured surfaces and (**B**) CHF (q''_{CHF}) as a function of maximum dry spot propagation area (A_{dm}). (**C**) Experimentally measured average bubble departure diameter (D_d) for both unmodified and structured surfaces as a function of pool boiling heat flux (q''). Exemplary top-view endoscopy photographs of the maximum dry spot propagation area for (**D**) nanograss, (**E**) nanobud, (**F**) nanoflower, and (**G**) nanopetal morphologies. The snapshots for all structured surfaces were captured at heat fluxes of ≈20 ± 2.5 W/cm^2. Time zero (τ = 0) in (A) and (B) represent the moment when the dry spot initiated. The image diameters of (D) to (G) are 1400, 1400, 1500, and 1600 μm, respectively.

on surfaces with lower dry spot areas show a smaller departure diameter (Fig. 4C), which governs CHF enhancement (*17*, *40*).

Having developed a fundamental understanding of the liquid film dynamics underneath bubbles during evolution, we now quantitatively analyze the relationship between liquid film evaporation and CHF. During pool boiling, CHF is triggered when neighboring vapor columns coalesce, and the dynamic equilibrium of liquid evaporation and replenishment is eliminated (*41*). At the occurrence of CHF, surface heat flux (q''_{CHF}) can be estimated using the rate of vapor generation perpendicular to the surface, which is expressed as

$$q''_{CHF} = h_{fg} u_g \rho_g \tag{1}$$

where h_{fg}, u_g, and ρ_g are the latent heat of vaporization, velocity of the generated vapor, and vapor density, respectively. The kinetic energy of the generated vapor at CHF can be considered as a separation mechanism between liquid and the surface due to its opposition to the force of gravity acting on the suspended liquid (*42*)

$$\rho_g u_g^2 \sim g(\rho_f - \rho_g)\lambda \tag{2}$$

where g denotes the gravitational acceleration and ρ_f is the liquid density. Here, λ represents the linear scale of capillary disturbances, which can be expressed as

$$\lambda = \sqrt{\sigma/[g(\rho_f - \rho_g)]} \tag{3}$$

where σ is the liquid-vapor surface tension. Therefore, the theoretical dimensionless prediction grouping for CHF based on hydrodynamic stability can be expressed as

$$K = \frac{q''_{CHF}}{\rho_g h_{fg}\left[\frac{\sigma g(\rho_f - \rho_g)}{\rho_g^2}\right]^{\frac{1}{4}}} \tag{4}$$

where K is a constant known as the dimensionless CHF. A number of models have proposed modifications to the dimensionless CHF based on various working conditions and surface properties, such as roughness, wettability, and wickability. The liquid retention capacity of the structures during bubble expansion plays a key role in enhancing CHF by replenishing liquid and delaying dry area formation, which also modifies the dimensionless CHF on structured surfaces.

As the liquid film on the structured surfaces evaporates (Fig. 5A), a dry spot forms near the nucleation site, initiating second-tier contact line propagation outward that approaches the first-tier three-phase contact line in the time interval τ_{CE}, which refers to the required time for complete evaporation of liquid film. Assuming a dry spot area A_d, the average evaporated volume flux from the liquid film can be evaluated as

$$u'_f = \frac{1}{A_d}\frac{\varepsilon A_d}{\tau_{CE}} = \frac{\varepsilon}{\tau_{CE}} \tag{5}$$

To quantify the influence of evaporated liquid flux from the structures on CHF, we define a dimensionless liquid retention number (Ret) following the dimensionless CHF format

$$\text{Ret} = \frac{\frac{\varepsilon}{\tau_{CE}}\rho_f}{\rho_g\left[\frac{\sigma g(\rho_f - \rho_g)}{\rho_g^2}\right]^{\frac{1}{4}}} \tag{6}$$

where Ret represents the ratio of transient evaporated mass flux of retained liquid within the structures to the critical mass flux of vapor leaving the surface due to complete evaporation. The liquid retention number characterizes the dimensionless contribution of liquid retention in the structures on CHF enhancement. Therefore, the dimensionless CHF for the structured surfaces can be expressed as

$$K_{structured} = K_{smooth} + C\text{Ret} \tag{7}$$

where $K_{structured}$ and K_{smooth} denote the dimensionless CHF for structured and smooth surfaces, respectively, and C is an unknown constant of proportionality, which can be empirically derived.

Figure 5B plots the experimentally measured CHF as a function of measured Ret for both smooth and modified surfaces. Fitting the

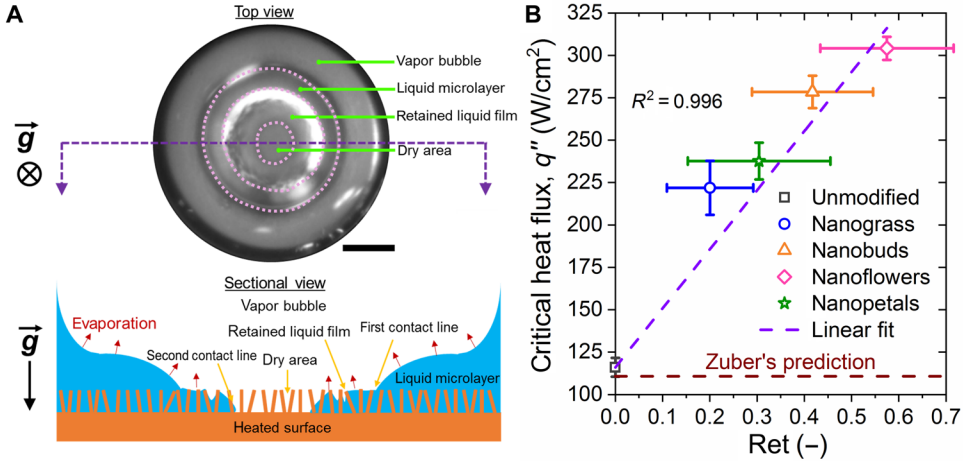

Fig. 5. CHF enhancement model. (**A**) Top: Top-view endoscopy image of a bubble base forming on a nanograss-structured CuO surface. Bottom: Schematic diagram of the bubble base on a structured surface. The length scale of the upper image and the lower diagram is not the same. The scale bar of the upper image represents 300 μm, while the lower schematic diagram is not to scale. (**B**) Experimentally measured CHF $\left(q''_{CHF}\right)$ as a function of the dimensionless liquid retention number (Ret) for the structured and unmodified surfaces studied here. The slope of the linear fit in (B) is 348.2 W/cm^2.

data shown in Fig. 5B to determine the linear relationship predicted by Eq. 7 results in a dimensionless CHF for smooth surfaces $K_{smooth} \approx 0.131$, which is the constant derived by Zuber seven decades ago (*36*). Simultaneously, the constant C is also obtained by fitting as $C \approx 3.14$. We note here that $C \approx \pi$ does not have a notable meaning as C represents a fitting coefficient, which varies according to specific experimental parameters such as surface and liquid properties and boiling conditions.

DISCUSSION

For the smooth Cu surface, no retained liquid film exists; hence, Ret = 0 and Eq. 7 simplifies to the classical Zuber prediction (*36*). The proposed model only considers the average evaporated volume flux of the retained liquid film during bubble evolution and is independent of specific surface parameters, such as structure length scale, structure material, and structure roughness, demonstrating its utility in predicting the CHF on structured surfaces with high liquid capacity. The inputs to the model do not consider structure parameters, as the key parameter is the experimentally measured ε/τ_{CE}, which is sensitive to surface structure geometry and chemistry. Furthermore, because the maximum dry spot propagation area for structured surfaces is inversely correlated with Ret, the proposed dimensionless Ret reflects the effect of dry area size induced by the retained liquid film underneath the bubble on CHF. Because the evaporated volume flux ε/τ_{CE} is needed to estimate Ret, the measurements of ε and τ_{CE} are important predictors of CHF. Water content is related to the surface morphology and porosity, which may be estimated without experiments by surface characterization methods for structured surfaces [such as scanning electron microscopy (SEM), atomic force microscopy, and Brunauer-Emmett-Teller]. However, the liquid film evaporation time τ_{CE} refers to the required time for complete evaporation of the liquid film, which is highly correlated to liquid retention capability of the surface, liquid properties, and experimental condition, such as system pressure, gravity, and heating condition. Therefore, at this point, it is too complex to estimate τ_{CE} via simple analysis of the surface morphology and chemistry without conducting any boiling tests. Because all of our endoscopic observations in this work were carried out at relatively lower heat fluxes (less than 20 ± 4 W/cm^2), and the observed evaporated volume flux (ε/τ_{CE}) has a linear relationship with the overall CHF, this provides a rapid approach to predicting CHF through liquid film analysis at a relatively low heat flux and relatively easy experimental conditions.

The linear positive correlation between Ret and CHF shows that the measured evaporated volume flux of liquid film (ε/τ_{CE}), which is related to the surface water retention capability and second-tier three-phase contact line propagation velocity during bubble growth, is critical to predicting CHF enhancement. Previous work has shown that improvement of surface wickability is the main reason for CHF enhancement on structured surfaces (*43*–*45*). To explore the relationships between CHF enhancement, surface wickability, and water retention capability, droplet spreading experiments to characterize surface wickability were performed on all modified surfaces developed here. Details concerning experimental setup can be found in section S2. As shown in Fig. 6 (A and B), the variation of CHF also shows a linear relationship with the Washburn wicking coefficient (*46*), signaling that the pool boiling performance on structured surfaces is governed by surface wickability, which appears to be in conflict with our conclusions demonstrating the linear relationship between CHF and evaporated volume flux (ε/τ_{CE}). These parallel conclusions arise because both surface wickability and water retention capability are determined by surface structure morphology, chemistry, and thickness. The fabricated nanostructures in this work are randomly formed on the Cu substrate, thus forming many interconnected capillary pathways within the structures. These interconnected spaces not only increase surface porosity and water retention capacity but also improve capillary action to enhance surface wickability. Therefore, as shown in Fig. 6C, the variation of water content and surface wicking capability are related.

Considering the relation between surface wickability and surface water content, we maintain that water content, rather than wickability, is the more relevant and widely applicable property of structured surfaces, which form liquid films under bubbles during growth. The propagation directions of the liquid film during bubble growth and departure governed by these two mechanisms differ. Because of the capillary force at the three-phase interface, the liquid is driven from the microlayer area to the dry area. Hence, the propagation direction of the liquid film induced by surface wickability should be from outside toward the bubble center. However, as shown in Fig. 3D and movies S2 to S5, the second-tier three-phase contact lines within the structures on all modified surfaces propagate from the center of the bubble periphery, indicating that the liquid film exists before the appearance of the dry area. Furthermore, the propagation distances of the liquid film for these two conditions differ. Because of the relatively high temperature in the dry area, the liquid absorbed from the microlayer area will rapidly evaporate, leading to the absorbed liquid film being restricted near the microlayer. However, the liquid film observed in our studies covers the entire dry area, confirming the hypothesis that liquid film is formed by liquid retention in the structures. In addition, the propagation time scales are different when comparing retained liquid and wickability-mediated capillary flows. As shown in Fig. 3 (D and E), from bubble generation to complete propagation of the first-tier contact line, 1 ms elapses to form a liquid film with a diameter of ≈1 mm. In contrast, for these rapid time scales, the capillary distance is only ≈ 0.05 mm (Fig. 6A), which is far shorter than the diameter of actual liquid film underneath the bubble base. Hence, although a linear fitting relationship exists between water content and Washburn wicking coefficient, the water retention capability of the structured surfaces governs liquid film dynamics and presents a more versatile experimental measure, which can predict CHF for any structured surface morphology.

To put our hypothesis to the test, we propose an experiment where the surface wickability remains constant, while the retention capability changes. To achieve these conflicting requirements, we rationalize that surface structures that have discrete subtractive features (voids) with a lack of interconnection between each other will achieve the hypothesized requirement. This rationalization stems from the fact that void features enhance retention capacity while also not enabling wicking because of the lack of interconnection from one to another. To fabricate the proposed structures, we formed hierarchical micro/nanostructured surfaces using a two-step method involving stamping and chemical etching (Fig. 6, D to F). The surface fabrication and characterization details can be found in section S3. Briefly, a sample with an array of nickel-based micropyramids having base lengths of 122 μm and heights of 45 μm was used as a template and stamped vertically on thoroughly cleaned Cu surfaces with different pressures varying from 5 to 30 kN/cm^2. The dimensions of the

obtained Cu-based inverse pyramids, including the base length and depth, vary with the stamping pressure. After stamping, the surfaces were coated with the nanograss CuO layer using the chemical etching method to further enhance liquid retention capability. The resulting hierarchical inverse pyramid (HIP)–structured surfaces were differentiated as "HIP36," "HIP46," and "HIP67" due to their differing base lengths of 36, 46, and 67 μm, respectively. Because of the discrete nature of the inverse pyramids, their contribution to capillary action is negligible and the measured droplet wicking propagation distance on the hierarchical structured surfaces is similar to that on the nanograss-structured surface (Fig. 6G). However, the existence of the discrete structures improves liquid retention capability due to the increase of nanograss-covered surface area and the presence of macroscale stamped pits. Boiling curves on the HIP-structured surfaces are shown in Fig. 6H. The CHF achieved on the HIP with a base length of 36 μm (HIP36) is slightly higher compared to the plane nanograss–structured surface. With the increasing base length of the inverse pyramid, the obtained CHF is

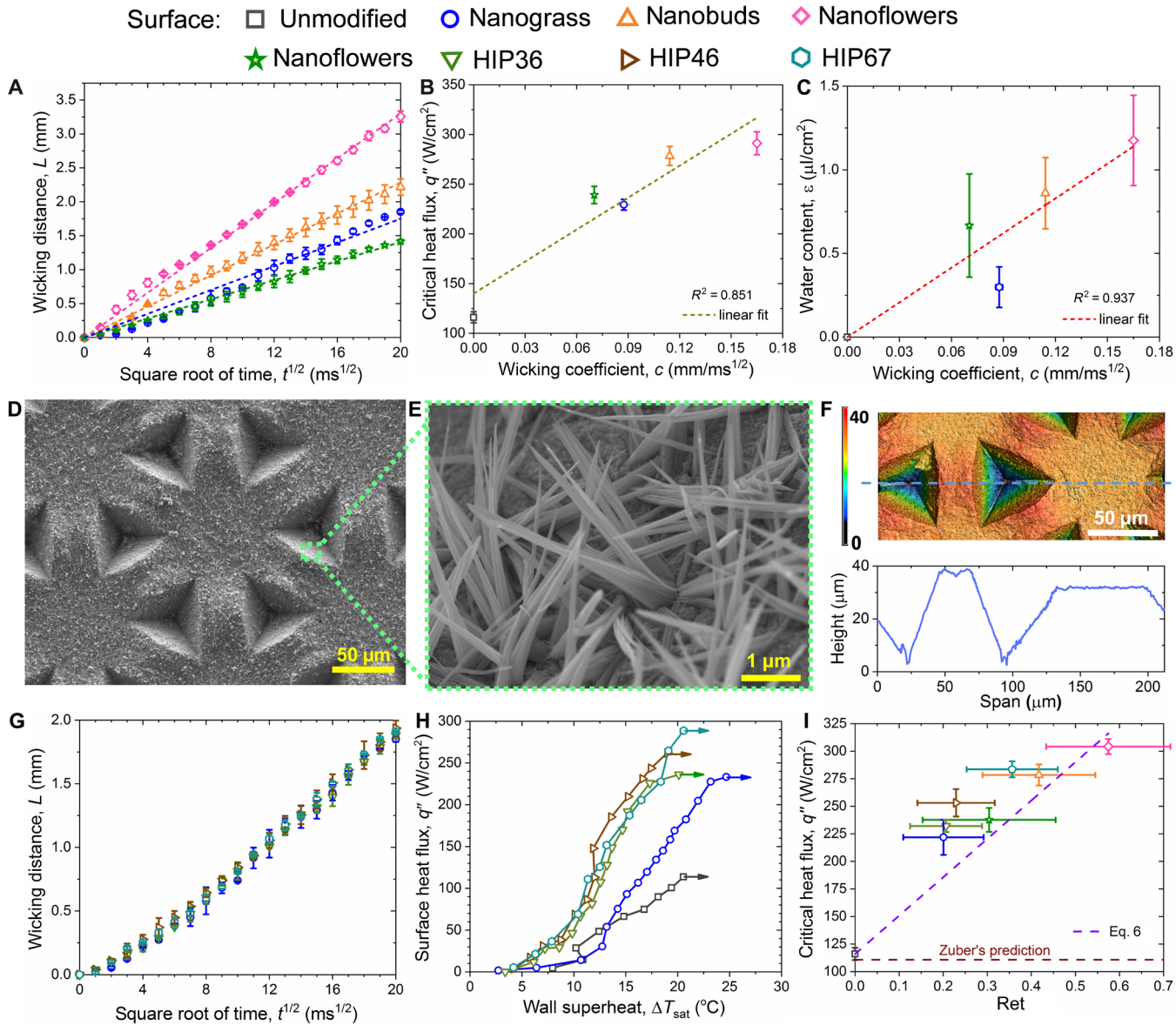

Fig. 6. Pool boiling performance of hierarchical inverse pyramidal structured surfaces. (**A**) Wicking distance (*L*) of the structured surfaces with nanograss, nanobud, nanoflower, and nanopetal morphologies as a function of the root of time ($t^{1/2}$). (**B**) CHF as a function of Washburn wicking coefficient. (**C**) Water content (ε) as a function of the Washburn wicking coefficient (*c*) for the various structured surfaces studied here. The slopes of the linear fits in (B) and (C) are 338 $W{\cdot}s^{1/2}/cm^3$ and 0.69 $nl/[cm{\cdot}(m{\cdot}s)^{1/2}]$, respectively. (**D**) Top-view SEM image of the HIP-structured surface with a base length of 46 μm, with (**E**) magnified area [green dotted box in (D)] showing the conformal nanograss structures. (**F**) Three-dimensional optical-profilometry height map of the inverse pyramid structures (top) and the corresponding surface profile along the blue dashed axis line (bottom). (**G**) Wicking distances (*L*) of the nanograss-structured surface and HIP-structured surfaces as a function of square root of time ($t^{1/2}$). (**H**) Boiling curves on the unmodified, nanograss-structured, and HIP-structured surfaces. (**I**) CHF as a function of dimensionless liquid retention number Ret for all data. The linear fit to the data in (A) to (C) was obtained using a least squares fitting algorithm. See section S3 for fitting details.

gradually enhanced. The modified liquid retention capability of the HIP-structured surfaces was estimated on the basis of the dimension of inverse pyramid and water content of nanograss surface. The detailed estimation process can be found in section S3. As shown in Fig. 6I, the CHF on the HIP-structured surfaces as a function of dimensionless liquid retention number Ret is consistent with the model obtained from the nanostructured surfaces, with a slight deviation due to the increase in nucleation site density created by the stamped pits. Because of the similar wicking capability of these hierarchical structures (fig. S5), the CHFs on the HIP-structured surfaces deviate notably from the linear tendency previously obtained between CHF and the Washburn wicking coefficient. The discrepancy confirms our hypothesis that, compared to the surface wickability, the liquid retention capability of the structured surface plays a more versatile predictive role on predicting boiling heat transfer performance.

Although our experiment fails to disprove our hypothesis that liquid retention capability governs thin liquid film dynamics and CHF, surface wickability plays an important role in boiling heat transfer enhancement, especially for pool boiling and thin liquid film boiling on structured surface with interconnected pores. As shown in Fig. 3 (C and D, iv), when the propagation radius of the second-tier contact line reaches its maximum at $\tau = 5.7$ ms, the second-tier contact line does not coincide with the first-tier contact line. A banded liquid film gap remains between the two contact lines, which is created by capillary wicking from the bulk liquid to the dry area in the structures (*37*). This result indicates that wickability plays an important role in enhancing heat transfer by providing additional pathways for liquid replenishment during bubble growth. Because water retention capability and surface wickability are related and both are governed by capillary pressure within structures, surface wickability remains a valid metric understanding pool boiling on structured surfaces with interconnected pores. However, surface wickability fails to reliably predict CHF enhancement on structured surfaces with independent pores, where surface water content is more versatile at capturing the important mechanisms governing boiling heat transfer. It is worth noting that, as shown in Figs. 2D and 6B, when the wicking coefficient or water content is nearly zero, the predicted CHF does not exactly match with the experimental values on unmodified surfaces. The structures may affect heat transfer performance in other ways besides improving surface wickability and evaporated volume flux, such as improving surface wettability, increasing nucleation site density, and changing surface roughness.

The evaporated volume flux ε/τ_{CE} used in Eq. 6 is determined by analyzing the water content ε and liquid film evaporation time τ_{CE}. Because the evaporation time is related to the specific structure thickness, porosity, morphology, chemistry, as well as the liquid thermophysical properties and experimental conditions, the evaporated volume flux is difficult to calculate without the use of experimental inputs. Furthermore, a trade-off exists between water content and evaporation time. As the thickness of the porous structure increases, water content improves. However, thicker structures increase the conduction thermal resistance between the heated substrate and structure surface exposed to the liquid (*12*, *17*), thus reducing evaporation within structures and lengthening τ_{CE}. Furthermore, even if the thickness and porosity of the structures are identical, the effective cross-plane thermal resistance is notably affected by structure features, such as pore diameters, tortuosity, interconnectedness, and pore neck diameter, thus affecting the experimentally observed evaporation time (*47*). Therefore, the evaporated volume flux does not increase monotonically, indicating the existence of an upper limit for CHF enhancement using the model developed here. In the future, it would be interesting to investigate the effects of structure thickness on CHF and explore the variation of liquid film evaporation dynamics on structures with different thicknesses as well as porosity and morphology. Although the predictions of the modified hydrodynamic instability model show good agreement with the experimental results, our model is limited due to the need to experimentally measure ε/τ_{CE}. For structured surfaces devoid of nonporous structures, e.g., microchannels and micropillars, water retention during bubble evolution is relatively poor. The observed liquid film ring is governed mainly because of the high capillary pressure gradient induced by the concave meniscus in the ultrasmall channels (*37*). The CHF enhancement on these microchannel or micropillar surfaces mainly occurs due to the length augmentation of the three-phase contact line (*23*, *24*, *37*, *48*). Hence, our modified model is not applicable to these structures and needs to be used with caution.

In summary, we have used micro/nanostructured surfaces to study CHF enhancement mechanisms during pool boiling of water. Variable magnification in-liquid endoscopy was used to achieve in situ visualization of the three-phase contact line dynamics during bubble evolution. We observe the previously unidentified coexistence of two three-phase contact lines underneath growing bubbles on structured surfaces. The transition between the two contact lines is defined by the thin liquid film retained within structures and formed mainly because of the disparate advancing velocity of the two contact lines. To quantitatively analyze the relationship between the thin liquid film in the structures and CHF enhancement, a modified hydrodynamic instability model is developed on the basis of observed liquid film evaporation dynamics. We demonstrate the criticality of dimensionless liquid retention number Ret as the key parameter for predicting pool boiling CHF on structured surfaces and compare our results with classical wickability formulations, demonstrating previously unidentified limitations with currently well-established frameworks. Our work outlines design guidelines for the holistic optimization of boiling heat transfer surfaces, which has important implications for a wide variety of applications.

MATERIALS AND METHODS

Structured surface fabrication and characterization

The structures were prepared on Cu substrates via chemical etching in an ammonium ambient solution. The developed structures have demonstrated excellent performance for thermofluidic applications including condensation and frosting (*49*–*53*). Briefly, the Cu samples (purity, 99.9%, 110 Cu, McMaster) with sizes of 15 mm × 15 mm were first polished using #400 and #2000 sandpaper sequentially to remove macroscale scratches and ensure similar roughness. After polishing, the Cu samples were rinsed thoroughly with dilute hydrochloric acid (2 M, CAS no. 7647-01-0, Sigma-Aldrich), acetone (CAS no. 67-64-1, Sigma-Aldrich), and distilled water (CAS no. 7732-18-5, Sigma-Aldrich). Next, the cleaned Cu samples were immersed into an ammonium ambient solution made from a mixture of aqueous 2.5 M sodium hydroxide (NaOH, CAS no. 1310-73-2, Sigma-Aldrich) and 0.1 M ammonium persulfate [$(NH_4)_2S_2O_8$, CAS no. 7727-54-0, Sigma-Aldrich] at a constant temperature ranging from 5° to 85°C for 5 or 30 min. Then, the oxidized $Cu(OH)_2$ samples

were rinsed thoroughly with distilled water and dried in a clean nitrogen stream. Subsequently, the samples were heated in an atmospheric pressure furnace (Lindberg/Blue M BF51732C-1, Thermo Fisher Scientific Co.) with a constant temperature of 180°C for 2 hours to complete the transformation to CuO structures via dehydration. The surface structures were varied by altering the etching temperature and time. Specifically, the nanograss and nanobud structures were fabricated at temperatures of 5° and 25°C for 5 min, respectively. The nanoflower and nanopetal structures were prepared at temperatures of 45° and 85°C for 30 min, respectively. Before characterization and testing, the margins (edges) of the prepared samples were polished using #400 and #2000 sandpaper sequentially, thus leaving the central area (10 mm × 10 mm) to remain structured.

XPS characterization

XPS data were obtained using a Kratos Analytical Axis Ultra with a monochromatic Al Kα x-ray source. The size of the analyzed region was 0.2 mm × 0.5 mm. The instrument was maintained at a pressure of 10^{-7} Pa during the experiments. The spectra were post-processed with Casa XPS software (Casa Software Ltd.). The C 1s binding energy (284.8 eV) of carbon was used as a calibration to compensate for charging effects.

Pool boiling tests

The pool boiling setup consists of a pool boiling chamber made of clear polycarbonate (Acme Plastics), a heating system with five cartridge heaters (J3A-15429, Instrumart), a high-speed camera (Fastcam Mini AX200, Photron), and an endoscope (Hawkeye Pro Hardy 17″, Gradient Lens Corporation). Distilled water (CAS no. 7732-18-5, Aqua Solutions) in the chamber is heated up to the saturation temperature using four immersion heaters (L4E-11290, Instrumart) during experiments. A proportional-integral-differential controller (PM3C1CA-AAAAAAA, Instrumart) with a resistance temperature detector (B-PX1126Y-LR4P39T2S, Reotemp Instruments) is used to measure and monitor the water temperature. To ensure that the heat generated by the cartridge heaters is transferred in the axial direction, the heating system is insulated using a porous ceramic and Teflon. Three thermocouples [TJC36-CAIN-020(G)-6, OMEGA] are installed along the axis of Cu block with intervals of 8 mm, and the distance between the top thermocouple and the sample is 3 mm. During boiling experiments, the endoscope was used to observe and record contact line and liquid film dynamics.

Solder (7758A3, McMaster-Carr) with a thermal conductivity of ≈50 W/(m·K) was used to fix the test samples to the upper surface of the Cu heater block. Briefly, the cartridge heaters were first turned on to heat the surface to approximately 190°C. A piece of solder with a mass of 1.5 g was placed on the heated surface and spread into a liquid film. The heaters were then de-energized after placing the sample on the liquid film. The sample was then soldered on the Cu block when the surface cooled down, and the thickness of the solder layer was approximately 200 μm as characterized via cross-sectioning and optical microscopy. The sides of the samples were coated with an insulating epoxy (EPO-TEK-930-4, Epoxy Technology Inc.) to seal the samples. To remove the influence from the surrounding sealing hydrophobic epoxy on liquid supply to the structured surface during pool boiling, all samples were designed to have a face area of 15 mm × 15 mm, resulting in a slightly larger size than the central structured area (10 mm × 10 mm).

Before conducting the experiments, the deionized water in the chamber was heated up to the saturation point in ambient conditions (100°C) and then degassed by allowing continual heating for approximately 30 min. During the experiments, the input power is incrementally increased and the thermocouple readings were recorded after the system reached steady state. Each data point had a steady state time constant of about 1 hour, making the acquisition of a single sample pool boiling curve take approximately 24 hours. The surface heat flux and temperature were calculated by Eqs. 8 and 9, respectively

$$q'' = -k_{Cu}\left(\frac{3T_1 - 4T_2 + T_3}{2\Delta x}\right) \tag{8}$$

where q'' is the heat flux, k_{Cu} is the temperature-dependent thermal conductivity of the Cu heater block, and Δx is the distance between the thermocouples in the Cu calorimeter bar.

$$T_{surface} = T_1 - q''\left(\frac{x_0 + \delta_1}{k_{Cu}} + \frac{\delta_2}{k_{solder}}\right) \tag{9}$$

where x_0 is the distance between the upper thermocouple and the top surface of the Cu bar, δ_1 is the thickness of Cu sample, and δ_2 and k_{solder} are the thickness and thermal conductivity of the solder, respectively.

Water content characterization

The water retention capacity (ε, Fig. 1K) of the structured surfaces was characterized using a lubricant infusion method (*35*). That is, the water content of the porous structures was estimated by weighting the mass difference before and after liquid infusion into the structures. Water content is difficult to characterize using water as the probe fluid because of the relatively large vapor pressure of water at room temperature and higher evaporation rate. Furthermore, the relatively low viscosity of water and its relatively high surface tension make it difficult to pin within the structures without any loss around the edges (due to wetting). Hence, we rationally selected vacuum-grade Krytox lubricant (Krytox VPF 1525) with a higher density, lower vapor pressure, and higher dynamic viscosity to increase the signal-to-noise ratio in the mass measurement. Greater measurement fidelity is achieved through limiting mass loss due to evaporation and ensuring complete filling of pores with limited gravitational drainage after removal of excess lubricant. Note that the samples used for boiling tests and water content characterization are independent of each other but fabricated using the same methods. Hence, the lubricant used for water content characterization was not present in any way during the boiling tests.

The fabricated structured samples were first immersed into the lubricant for 10 min and then positioned vertically at ambient conditions to remove the excess liquid by gravitational body forces. The mass difference (Δm) of the samples before and after lubricant immersion is equivalent to the mass of absorbed lubricant on the surface. The transient mass difference of the samples as a function of vertical resting time is shown in fig. S8. Because the mass differences of the samples after being positioned vertically for 24 hours remained constant, the mass difference at 24 hours was selected as the mass of absorbed lubricant within the structures. To avoid the influence of the lubricant film absorbed by the smooth surface, unmodified Cu surfaces were characterized as well to provide a

comparison, obtaining a similar mass difference (Δm_0). Hence, the water content (ε) of the structured surfaces was estimated as

$$\varepsilon = \varepsilon_l = \frac{\Delta m - \Delta m_0}{\rho_l A} \quad (10)$$

where ε_l denotes the lubricant content of structured surfaces after immersion in the lubricant, ρ_l represents the density of lubricant, and A is the structured surface sample projected area. Three individual samples for each structured surface were tested to reduce measurement uncertainty of surface water content due to the slight differences between surface preparation and lubricant infusion processes from sample to sample. The measured values of water contents for all structured surfaces refer to the mean values of these three independent measurements. It is worth noting that the liquid retention capability of the micro/nanostructures is due to their excellent capacity to generate high capillary pressure and good capillarity (*35*, *54*). However, for surfaces with macroscale and millimeter-scale structures, the infused liquid can completely drain from the surface as little liquid retention capability exists for large structures because of the lack of capillary pressure generated within the pores (*55*).

SUPPLEMENTARY MATERIALS

Supplementary material for this article is available at http://advances.sciencemag.org/cgi/content/full/7/26/eabg4537/DC1

REFERENCES AND NOTES

1. J. Kim, Review of nucleate pool boiling bubble heat transfer mechanisms. *Int. J. Multiphase Flow* **35**, 1067–1076 (2009).
2. S. G. Kandlikar, A new perspective on heat transfer mechanisms and sonic limit in pool boiling. *J. Heat Transfer* **141**, 051501 (2019).
3. S. Mori, Y. Utaka, Critical heat flux enhancement by surface modification in a saturated pool boiling: A review. *Int. J. Heat Mass Transfer* **108**, 2534–2557 (2017).
4. H. J. Cho, D. J. Preston, Y. Zhu, E. N. Wang, Nanoengineered materials for liquid–vapour phase-change heat transfer. *Nat. Rev. Mater.* **2**, 16092 (2016).
5. D. E. Kim, D. I. Yu, D. W. Jerng, M. H. Kim, H. S. Ahn, Review of boiling heat transfer enhancement on micro/nanostructured surfaces. *Exp. Therm. Fluid Sci.* **66**, 173–196 (2015).
6. L.-W. Fan, J.-Q. Li, D.-Y. Li, L. Zhang, Z.-T. Yu, K.-F. Cen, The effect of concentration on transient pool boiling heat transfer of graphene-based aqueous nanofluids. *Int. J. Therm. Sci.* **91**, 83–95 (2015).
7. L.-W. Fan, J.-Q. Li, Y.-Z. Wu, L. Zhang, Z.-T. Yu, Pool boiling heat transfer during quenching in carbon nanotube (CNT)-based aqueous nanofluids: Effects of length and diameter of the CNTs. *Appl. Therm. Eng.* **122**, 555–565 (2017).
8. L.-W. Fan, J.-Q. Li, Y.-Y. Su, H.-L. Wang, T. Ji, Z.-T. Yu, Subcooled pool film boiling heat transfer from spheres with superhydrophobic surfaces: An experimental study. *J. Heat Transfer* **138**, 021503 (2016).
9. R. Li, Z. Huang, A new CHF model for enhanced pool boiling heat transfer on surfaces with micro-scale roughness. *Int. J. Heat Mass Transfer* **109**, 1084–1093 (2017).
10. K.-H. Chu, R. Enright, E. N. Wang, Structured surfaces for enhanced pool boiling heat transfer. *Appl. Phys. Lett.* **100**, 241603 (2012).
11. A. Zou, D. P. Singh, S. C. Maroo, Early evaporation of microlayer for boiling heat transfer enhancement. *Langmuir* **32**, 10808–10814 (2016).
12. M. Tetreault-Friend, R. Azizian, M. Bucci, T. McKrell, J. Buongiorno, M. Rubner, R. Cohen, Critical heat flux maxima resulting from the controlled morphology of nanoporous hydrophilic surface layers. *Appl. Phys. Lett.* **108**, 243102 (2016).
13. R. Chen, M. C. Lu, V. Srinivasan, Z. Wang, H. H. Cho, A. Majumdar, Nanowires for enhanced boiling heat transfer. *Nano Lett.* **9**, 548–553 (2009).
14. Q. Wang, R. Chen, Ultrahigh flux thin film boiling heat transfer through nanoporous membranes. *Nano Lett.* **18**, 3096–3103 (2018).
15. H. Ze, F. Wu, S. Chen, X. Gao, Superhydrophilic composite structure of copper microcavities and nanocones for enhancing boiling heat transfer. *Adv. Mater. Interfaces* **7**, 2000482 (2020).
16. K.-H. Chu, Y. Soo Joung, R. Enright, C. R. Buie, E. N. Wang, Hierarchically structured surfaces for boiling critical heat flux enhancement. *Appl. Phys. Lett.* **102**, 151602 (2013).
17. J. Li, W. Fu, B. Zhang, G. Zhu, N. Miljkovic, Ultrascalable three-tier hierarchical nanoengineered surfaces for optimized boiling. *ACS Nano* **13**, 14080–14093 (2019).
18. N. S. Dhillon, J. Buongiorno, K. K. Varanasi, Critical heat flux maxima during boiling crisis on textured surfaces. *Nat. Commun.* **6**, 8247 (2015).
19. A. Jaikumar, S. G. Kandlikar, Ultra-high pool boiling performance and effect of channel width with selectively coated open microchannels. *Int. J. Heat Mass Transfer* **95**, 795–805 (2016).
20. R. Wen, Q. Li, W. Wang, B. Latour, C. H. Li, C. Li, Y.-C. Lee, R. Yang, Enhanced bubble nucleation and liquid rewetting for highly efficient boiling heat transfer on two-level hierarchical surfaces with patterned copper nanowire arrays. *Nano Energy* **38**, 59–65 (2017).
21. F. Wu, H. Ze, S. Chen, X. Gao, High-efficiency boiling heat transfer interfaces composed of electroplated copper nanocone cores and low-thermal-conductivity nickel nanocone coverings. *ACS Appl. Mater. Interfaces* **12**, 39902–39909 (2020).
22. R. Wen, X. Ma, Y.-C. Lee, R. Yang, Liquid-vapor phase-change heat transfer on functionalized nanowired surfaces and beyond. *Joule* **2**, 2307–2347 (2018).
23. P. A. Raghupathi, S. G. Kandlikar, Pool boiling enhancement through contact line augmentation. *Appl. Phys. Lett.* **110**, 204101 (2017).
24. H. Kim, H. S. Ahn, H. J. Kwak, M. H. Kim, D. E. Kim, Boiling crisis controlled by capillary pumping and viscous friction: Liquid penetration length and dry spot diameter. *Appl. Phys. Lett.* **109**, 243901 (2016).
25. H. S. Ahn, C. Lee, J. Kim, M. H. Kim, The effect of capillary wicking action of micro/nano structures on pool boiling critical heat flux. *Int. J. Heat Mass Transfer* **55**, 89–92 (2012).
26. W. Li, Z. Wang, F. Yang, T. Alam, M. Jiang, X. Qu, F. Kong, A. S. Khan, M. Liu, M. Alwazzan, Y. Tong, C. Li, Supercapillary architecture-activated two-phase boundary layer structures for highly stable and efficient flow boiling heat transfer. *Adv. Mater.* **32**, 1905117 (2020).
27. D. I. Yu, H. J. Kwak, H. Noh, H. S. Park, K. Fezzaa, M. H. Kim, Synchrotron x-ray imaging visualization study of capillary-induced flow and critical heat flux on surfaces with engineered micropillars. *Sci. Adv.* **4**, e1701571 (2018).
28. I.-C. Chu, H. C. No, C.-H. Song, Visualization of boiling structure and critical heat flux phenomenon for a narrow heating surface in a horizontal pool of saturated water. *Int. J. Heat Mass Transfer* **62**, 142–152 (2013).
29. Z. Chen, X. Hu, K. Hu, Y. Utaka, S. Mori, Measurement of the microlayer characteristics in the whole range of nucleate boiling for water by laser interferometry. *Int. J. Heat Mass Transfer* **146**, 118856 (2020).
30. C. Gerardi, J. Buongiorno, L. W. Hu, T. McKrell, Infrared thermometry study of nanofluid pool boiling phenomena. *Nanoscale Res. Lett.* **6**, 232 (2011).
31. C. Gerardi, J. Buongiorno, L.-W. Hu, T. McKrell, Study of bubble growth in water pool boiling through synchronized, infrared thermometry and high-speed video. *Int. J. Heat Mass Transfer* **53**, 4185–4192 (2010).
32. M. Bucci, A. Richenderfer, G.-Y. Su, T. McKrell, J. Buongiorno, A mechanistic IR calibration technique for boiling heat transfer investigations. *Int. J. Multiphase Flow* **83**, 115–127 (2016).
33. S. Ridwan, M. McCarthy, Nanostructure-supported evaporation underneath a growing bubble. *ACS Appl. Mater. Interfaces* **11**, 12441–12451 (2019).
34. H. Geistlinger, I. Ataei-Dadavi, S. Mohammadian, H. J. Vogel, The impact of pore structure and surface roughness on capillary trapping for 2-D and 3-D porous media: Comparison with percolation theory. *Water Resour. Res.* **51**, 9094–9111 (2015).
35. S. Sett, P. Sokalski, K. Boyina, L. Li, K. F. Rabbi, H. Auby, T. Foulkes, A. Mahvi, G. Barac, L. W. Bolton, N. Miljkovic, Stable dropwise condensation of ethanol and hexane on rationally designed ultrascalable nanostructured lubricant-infused surfaces. *Nano Lett.* **19**, 5287–5296 (2019).
36. N. Zuber, *Hydrodynamic Aspects of Heat Transfer* (Ramo-Wooldridge Corp., University of California, Los Angeles, 1959).
37. J. Li, G. Zhu, D. Kang, W. Fu, Y. Zhao, N. Miljkovic, Endoscopic visualization of contact line dynamics during pool boiling on capillary-activated copper microchannels. *Adv. Funct. Mater.* **31**, 2006249 (2020).
38. M. Matkovič, B. Končar, Bubble departure diameter prediction uncertainty. *Sci. Technol. Nucl. Install.* **2012**, 863190 (2012).
39. A. Faghri, Y. Zhang, Boiling, in *Fundamentals of Multiphase Heat Transfer and Flow* (Springer International Publishing, 2020).
40. R. Cole, Bubble frequencies and departure volumes at subatmospheric pressures. *Aiche J.* **13**, 779–783 (1967).
41. W. M. Rohsenow, P. Griffith, *Correlation of Maximum Heat Flux Data for Boiling of Saturated Liquids* (Massachusetts Institute of Technology, Division of Industrial Cooperation, 1955).
42. S. S. Kutateladze, On the transition to film boiling under natural convection. *Kotloturbostroenie* **3**, 10–12 (1948).
43. M. M. Rahman, E. Olceroglu, M. McCarthy, Role of wickability on the critical heat flux of structured superhydrophilic surfaces. *Langmuir* **30**, 11225–11234 (2014).
44. J.-Q. Li, L.-W. Mou, J.-Y. Zhang, Y.-H. Zhang, L.-W. Fan, Enhanced pool boiling heat transfer during quenching of water on superhydrophilic porous surfaces: Effects of the surface wickability. *Int. J. Heat Mass Transfer* **125**, 494–505 (2018).

45. J.-Q. Li, J.-Y. Zhang, L.-W. Mou, Y.-H. Zhang, L.-W. Fan, Enhanced transitional heat flux by wicking during transition boiling on microporous hydrophilic and superhydrophilic surfaces. *Int. J. Heat Mass Transfer* **141**, 835–844 (2019).
46. E. W. Washburn, The dynamics of capillary flow. *Phys. Rev.* **17**, 273–283 (1921).
47. H. C. Chang, M. C. Rajagopal, M. J. Hoque, J. Oh, L. Li, J. Li, H. Zhao, G. Kuntumalla, S. Sundar, Y. Meng, C. Shao, P. M. Ferreira, S. M. Salapaka, S. Sinha, N. Miljkovic, Composite structured surfaces for durable dropwise condensation. *Int. J. Heat Mass Transfer* **156**, 119890 (2020).
48. S. Poudel, A. Zou, S. C. Maroo, Evaporation dynamics in buried nanochannels with micropores. *Langmuir* **36**, 7801–7807 (2020).
49. X. Chen, L. Kong, D. Dong, G. Yang, L. Yu, J. Chen, P. Zhang, Fabrication of functionalized copper compound hierarchical structure with bionic superhydrophobic properties. *J. Phys. Chem. C* **113**, 5396–5401 (2009).
50. J. Y. Lee, S. Pechook, B. Pokroy, J. S. Yeo, Multilevel hierarchy of fluorinated wax on CuO nanowires for superoleophobic surfaces. *Langmuir* **30**, 15568–15573 (2014).
51. A. Chaudhary, H. C. Barshilia, Nanometric multiscale rough CuO/$Cu(OH)_2$ superhydrophobic surfaces prepared by a facile one-step solution-immersion process: Transition to superhydrophilicity with oxygen plasma treatment. *J. Phys. Chem. C* **115**, 18213–18220 (2011).
52. J. Feng, Y. Pang, Z. Qin, R. Ma, S. Yao, Why condensate drops can spontaneously move away on some superhydrophobic surfaces but not on others. *ACS Appl. Mater. Interfaces* **4**, 6618–6625 (2012).
53. Q. Hao, Y. Pang, Y. Zhao, J. Zhao, J. Zhang, J. Feng, S. Yao, Mechanism of delayed frost growth on superhydrophobic surfaces with jumping condensates: More than interdrop freezing. *Langmuir* **30**, 15416–15422 (2014).
54. H.-H. Tran, Y. Kim, C. Ternon, M. Langlet, D. Riassetto, Lubricant depletion-resistant slippery liquid-infused porous surfaces via capillary rise lubrication of nanowire array. *Adv. Mater. Interfaces* **8**, 2002058 (2021).
55. P. Kim, M. J. Kreder, J. Alvarenga, J. Aizenberg, Hierarchical or not? Effect of the length scale and hierarchy of the surface roughness on omniphobicity of lubricant-infused substrates. *Nano Lett.* **13**, 1793–1799 (2013).

Acknowledgments: SEM was carried out in the Materials Research Laboratory Central Facilities, University of Illinois. **Funding:** J.L. and N.M. acknowledge funding support from the Office of Naval Research under grant no. N00014-16-1-2625. The authors also acknowledge funding support from the National Science Foundation under award no. 1554249. N.M. acknowledges funding support from the International Institute for Carbon Neutral Energy Research (WPI-I2CNER), sponsored by the Japanese Ministry of Education, Culture, Sports, Science, and Technology. **Author contributions:** J.L. and N.M. conceived the initial idea for this research. N.M. guided the work. J.L., L.F., D.K., X.F., and X.Y. prepared and characterized the experimental samples. J.L., D.K., and W.F. carried out the pool boiling experiments and analyzed the data. J.L. and N.M. carried out the theoretical analysis. J.L. and N.M. wrote the manuscript. All the authors have given approval to the final version of the manuscript. **Competing interests:** The authors declare that they have no competing interests. **Data and materials availability:** All data needed to evaluate the conclusions in the paper are present in the paper and/or the Supplementary Materials.

Submitted 7 January 2021
Accepted 14 May 2021
Published 25 June 2021
10.1126/sciadv.abg4537

Citation: J. Li, D. Kang, K. Fazle Rabbi, W. Fu, X. Yan, X. Fang, L. Fan, N. Miljkovic, Liquid film–induced critical heat flux enhancement on structured surfaces. *Sci. Adv.* **7**, eabg4537 (2021).